Article

Screening chronic kidney disease through deep learning utilizing ultra-wide-field fundus images

Check for updates

Xinyu Zhao[1,29], Xingwang Gu[1,29], Lihui Meng[1], Yongwei Chen[2], Qing Zhao[1], Shiyu Cheng[1], Wenfei Zhang[1], Tiantian Cheng[1], Chuting Wang[1], Zhengming Shi[1], Shengyin Jiao[2], Changlong Jiang[2], Guofang Jiao[3], Da Teng[4], Xiaolei Sun[5], Bilei Zhang[6], Yakun Li[7], Huiqin Lu[8], Changzheng Chen[9], Hao Zhang[10], Ling Yuan[11], Chang Su[12], Han Zhang[13], Song Xia[14], Anyi Liang[15], Mengda Li[16], Dan Zhu[17], Meirong Xue[18], Dawei Sun[19], Qiuming Li[20], Ziwu Zhang[21], Donglei Zhang[22], Hongbin Lv[23], Rishet Ahmat[24], Zilong Wang[25], Charumathi Sabanayagam [26], Xiaowei Ding[2,27] ✉, Tien Yin Wong[16,28] ✉ & Youxin Chen [1] ✉

To address challenges in screening for chronic kidney disease (CKD), we devised a deep learning-based CKD screening model named UWF-CKDS. It utilizes ultra-wide-field (UWF) fundus images to predict the presence of CKD. We validated the model with data from 23 tertiary hospitals across China. Retinal vessels and retinal microvascular parameters (RMPs) were extracted to enhance model interpretability, which revealed a significant correlation between renal function and RMPs. UWF-CKDS, utilizing UWF images, RMPs, and relevant medical history, can accurately determine CKD status. Importantly, UWF-CKDS exhibited superior performance compared to CTR-CKDS, a model developed using the central region (CTR) cropped from UWF images, underscoring the contribution of the peripheral retina in predicting renal function. The study presents UWF-CKDS as a highly implementable method for large-scale and accurate CKD screening at the population level.

Chronic kidney disease (CKD) has emerged as a prominent cause of preventable morbidity and mortality, posing a significant threat to global public health. In 2017, 697.5 million cases of all-stage CKD were recorded, with a global prevalence of 9.1%. An estimated 1.2 million people died from CKD, with projections suggesting that this number could rise to 2.2 million by 2040 in the best-case scenario[1–3]. The associated healthcare and socio-economic burdens have also become overwhelming. Patients who benefit from renal replacement therapy (RRT) comprise about 0.15% of the global population, but this small group can absorb 2–3% of the healthcare budget of some advanced countries[4]. Nonetheless, costs for CKD are not limited to the expensive RRT but also include nonrenal healthcare costs, costs not related to healthcare, and costs for patients with CKD who are not yet receiving RRT[5]. These results underscored the urgent need for early detection and intervention of CKD at the population level[6,7]. However, CKD screening remains a formidable challenge, even in high-income developed countries and in at-risk populations such as individuals with hypertension or diabetes[8,9]. The primary hurdle lies in the fact that routine CKD screening typically necessitates blood tests to measure the estimated glomerular filtration rate (eGFR), or urine samples to detect protein or albumin, not to mention the more invasive kidney biopsy[10]. Previous studies have reported that awareness among patients with CKD remains shockingly low, around

10%[11], and a CKD screening strategy focusing solely on at-risk populations would overlook more than 50% of CKD cases[12]. To address this, there is a pressing need for noninvasive, convenient, and highly precise clinical examinations and biomarkers.

The retina offers a unique opportunity to directly and non-invasively visualize human microcirculation. Current consensus recognizes structural, developmental, organizational, and physiological similarities between the eye and kidney[13]. Retinal microvascular abnormalities have been proposed as indicators of systemic microvascular damage and renal dysfunction, while reduced eGFR has also been linked to retinal vascular diseases[14–18]. As a result, there has been a growing interest in verifying the association between these two and quantitatively evaluating retinal microvascular parameters (RMPs) as predictive indicators of renal function[19]. However, existing research in this area faces several unresolved issues. First, although a general relationship between RMPs and renal function has been established, results remain inconclusive[20,21]. Second, prior studies have primarily focused on retinal vasculature within the 30–60° range of the posterior retina and have been restricted to manually selected vascular branches proximal to the optic disc[20,22]. Recent perspectives suggest that peripheral retinal vessels may exhibit even earlier changes than central retinal vessels, highlighting the potential clinical significance of ultra-wide-field (UWF) scanning laser

A full list of affiliations appears at the end of the paper. ✉e-mail: dingxiaowei@sjtu.edu.cn; wongtienyin@tsinghua.edu.cn; ChenYX@pumch.cn

ophthalmoscopy, capable of capturing the ocular fundus up to 200° in a single exposure. Third, the segmentation of vessels and the assessment of RMPs may benefit from quick and automated artificial intelligence-based processes[2], as opposed to traditional manual vessel marking methods like the Singapore I Vessel Assessment (SIVA) system[23]. However, arteriovenous segmentation in UWF fundus images remains relatively unexplored, primarily due to the extensive coverage of thinner blood vessels within the 200° UWF image. This makes the annotation process and algorithm development exceedingly time-consuming and challenging.

Sabanayagam et al.'s recent research demonstrated the comparable effectiveness of a retinal image-based deep learning algorithm (DLA) and traditional risk factor-based models for CKD detection, highlighting the potential of noninvasive retinal photography for screening[24]. In light of these challenges and findings, our study aims to develop a DLA for CKD screening using UWF fundus images and prospectively validate it across multicenter settings nationwide. We also explored the role of the peripheral retina in CKD prediction. Our approach provided a noninvasive, automated, accurate, and easily implementable solution for population-level CKD screening.

Results

General data
Initially, we collected a total of 123,585 UWF images from 41,469 patients. After excluding low-quality images and patients lacking the requisite renal function indicators, a total of 26,539 UWF fundus images, corresponding to 9133 patients with paired renal function data, were ultimately included in this study. The image screening process is outlined in Fig. 1. During the evaluation of the image quality inspection process, we got a mean inter-rater consistency score of 99.3% (95% CI: 97.8–99.8%) among the three ophthalmologists, the mean concordance of each expert with the gold standard was 99.7%, the kappa value between the AI algorithm and the three retinal specialists was 0.975 (Supplementary Table 1). A summary of the demographic characteristics of the enrolled patients can be found in Table 1. The internal dataset consisted of 23,313 UWF images paired with renal function indicators, which were randomly divided into training, validation, and test sets at a ratio of 70:15:15. The multicenter test dataset encompassed 3226 UWF images derived from 1352 patients. Among all the participants in the study, 2365 out of the 26,539 UWF images (8.91%) were associated with patients diagnosed with CKD+. Further details pertaining to the internal dataset and the multicenter test set can be found in Table 1.

Artery/vein segmentation
Our segmentation model, UNet++, could properly segment arteries, veins, and optic discs from UWF images. The DICE scores for each channel were 0.54, 0.61, and 0.88, respectively. The AUC scores were 0.74 (95% CI: 0.70–0.79), 0.80 (95% CI: 0.76–0.83), and 0.94 (95% CI: 0.91–0.98), respectively. When the segmentation is limited in the posterior fundus region, the DICE scores are 0.64, 0.70, and 0.88, respectively, and the AUC scores are 0.83 (95% CI: 0.81–0.85), 0.86 (95% CI: 0.84–0.88), and 0.94 (95% CI: 0.91–0.98), respectively. We randomly selected four UWF images for visualization of the segmentation results, as shown in Fig. 2. From the evaluation metrics and visualization results, the segmentation of the optic discs and the vessels was closely similar to the doctor's annotations.

Correlation between RMP and renal function
The results of the correlation analysis between the renal function indicators and retinal vascular metrics were summarized in Table 2. (1) For AVR, both B-AVR and C-AVR were significantly and negatively correlated with UCr, UA, and Urea (All $P < 0.05$). C-AVR was additionally negatively associated with UOB, UMAlb, Cr, and Alb (All $P < 0.05$). (2) For Df, both CTR-Df and UWF-Df were significantly and positively correlated with eGFR and UCr, while negatively correlated with UA, Cr, Urea, and Alb (All $P < 0.05$). UWF-Df was additionally positively correlated with UOB ($P < 0.05$), while CTR-Df was additionally negatively correlated with UMAlb and Alb ($P < 0.05$). (3) For TORT, we found eGFR and UCr were significantly and positively correlated with UWF-TORT (Both $P < 0.05$), while UMAlb, Cr, Urea, and Alb were negatively correlated with UWF-TORT (All $P < 0.05$). Interestingly, ACR was positively associated with CTR-TORT, while negatively associated with UWF-TORT (Both $P < 0.05$). (4) In Table 3, further evaluation found that the artery- and vein-Df of the UWF and central images were significantly correlated with most of the renal function indicators in different level ($P < 0.05$), except for UOB. Moreover, we also found Artery-UWF-Df showed the highest correlation coefficient with eGFR ($r = 0.31$, 95% CI 0.28–0.33), which was better than Artery-CTR-Df and Vein-UWF/CTR-Df. Generally, UWF-Df showed a better correlation than CTR-Df, while Artery-Df showed a better correlation than Vein-Df (Table 3 and Fig. 3).

Classification model results
We trained the UWF-CKDS to predict CKD status and use the CTR-CKDS for comparison. The performance metrics of these two models on the internal test set and multicenter test set were shown in Fig. 3. The
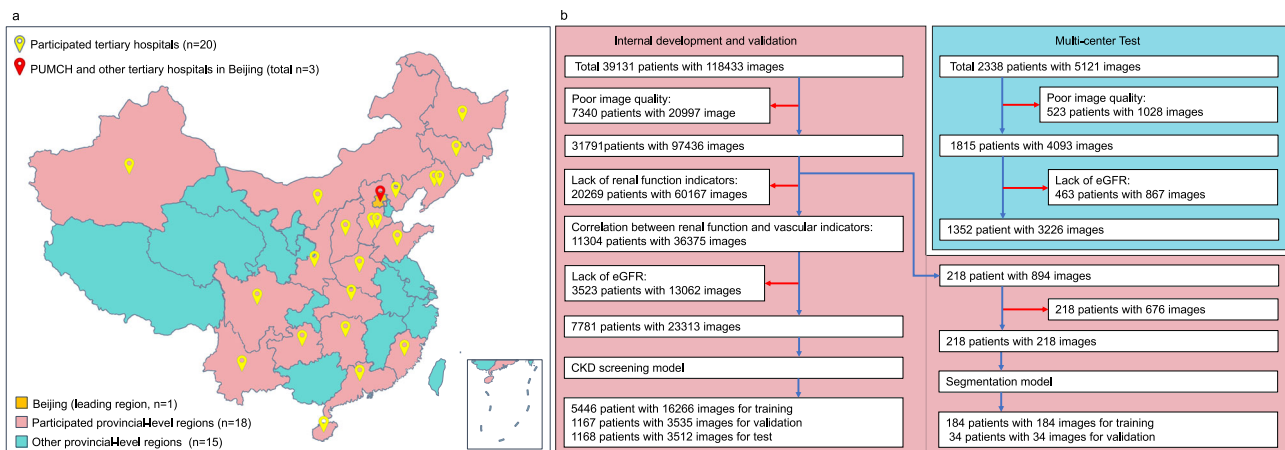
Fig. 1 | Patient data collection and screening process of the nationwide and multicenter study. a The 200° UWF images were captured, and the renal function and medical history items were prospectively extracted from 23 tertiary hospitals nationwide in China (See Supplementary Note 1 for detailed hospital information). **b** 123,585 UWF images from 41,469 patients were initially collected. 218 images from 218 patients were finally included for training the UWF image segmentation model. 23,313 images from 7781 patients were finally included for creating the CKD screening model in a 7:1.5:1.5 distribution for internal training, validation, and test. 3226 images from 1352 patients from multicenter collection were used for outer validation. Blue arrows: patients and images permitted to subsequent procedures. Red arrows: excluded patients and images according to the exclusion criteria.

Table 1 | Demographic data of enrolled patients and their distribution in study groups

Metric	General data	Internal dataset			Multicenter test
		Training set	Validation set	Test set	
Number of images, n (%)	26,539 (100%)	16,266 (61.29%)	3535 (13.32%)	3512 (13.23%)	3226 (12.16)
Number of patients, n (%)	9133 (100%)	5446 (64.48%)	1167 (13.82%)	1168 (13.83%)	1352 (16.01)
Images of CKD−/CKD+, n (times)	24,174/2365 (10.22)	14,994/1272 (11.79)	3249/286 (11.36)	3227/285 (11.32)	2704/522 (5.18)
Age, years (mean ± SD)	47.14 ± 18.31	45.82 ± 18.4	44.87 ± 18.15	47.42 ± 18.78	55.96 ± 14.56
Female, n (%)	14,285 (53.83%)	9120 (56.07%)	1915 (54.17%)	1779 (50.65%)	1471 (45.60%)
eGFR, mL/min/1.73 m² (mean ± SD)	97.48 ± 29.41	99.43 ± 29.12	99.43 ± 29.42	97.76 ± 28.49	85.18 ± 28.88
Previous medical history					
Diabetes, n (%)	6287 (23.69%)	3578 (22.0%)	767 (21.7%)	825 (23.49%)	1117 (34.62%)
Hypertension, n (%)	6911 (26.04%)	3830 (23.55%)	720 (20.37%)	924 (26.31%)	1437 (44.54%)
Cerebrovascular disease, n (%)	1739 (6.55%)	1023 (6.29%)	220 (6.22%)	227 (6.46%)	269 (8.34%)
Coronary heart disease, n (%)	1791 (6.75%)	934 (5.74%)	181 (5.12%)	227 (6.46%)	449 (13.92%)
Dyslipidemia, n (%)	4761 (17.94%)	2584 (15.89%)	496 (14.03%)	641 (18.25%)	1040 (32.24%)

CKD chronic kidney disease, *eGFR* estimated glomerular filtration rate.

Fig. 2 | Representation and comparison of image segmentation between experienced ophthalmology experts and UNet++ based segmentation model. Four UWF images (**a**) and the segmentation results from experienced ophthalmology experts (**b**) and the segmentation model (**c**) were randomly selected for representation. The automatic segmentation of the optic disc and the vessels were very close to the doctor's annotation.
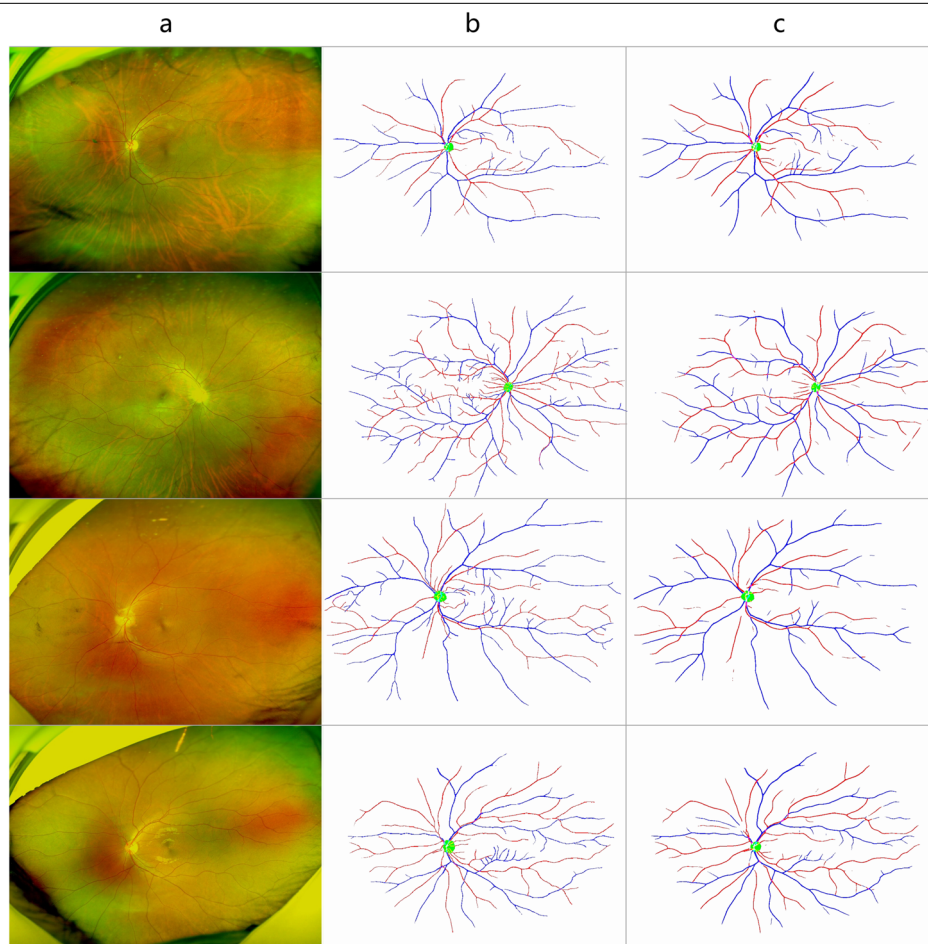
UWF-CKDS achieved higher AUC values than CTR-CKDS on both test datasets (internal 0.86 95% CI: 0.83–0.89 versus 0.82 95% CI: 0.79–0.86, $P < 0.01$; multicenter 0.81 95% CI: 0.76–0.86 versus 0.77 95% CI: 0.72–0.83, $P = 0.01$), demonstrating better predicting performance of UWF-CKDS over CTR-CKDS. Based on the analysis of the confusion matrix, UWF-CKDS showed higher sensitivity and a relatively lower specificity (Supplementary Fig. 1). When the sensitivity value was set at 0.80, UWF-CKDS showed significantly better specificity than CTR-CKDS in the multicenter test (0.69 95% CI: 0.65–0.71 versus 0.53 95% CI: 0.50–0.56, $P < 0.01$). In Fig. 4, the heatmaps showed the regions of interest of these two models. The UWF-CKDS focused not only on the posterior pole but also on the peripheral retinal area.

Table 2 | Correlation analysis between renal function indicators and retinal microvascular parameters

| Indicator	AVR				Df				TORT			
	B-AVR	P-value	C-AVR	P-value	CTR-Df	P-value	UWF-Df	P-value	CTR-TORT	P-value	UWF-TORT	P-value
eGFR	0.00 (−0.01 to 0.02)	0.480	0.00 (−0.01 to 0.02)	0.523	0.19 (0.17–0.21)	<0.001*	0.29 (0.27–0.31)	<0.001*	−0.01 (−0.02 to 0.00)	0.213	0.07 (0.05–0.08)	<0.001*
UCr (mmol/L)	−0.08 (−0.11 to −0.04)	<0.001*	−0.06 (−0.10 to −0.03)	<0.001*	0.11 (0.07–0.14)	<0.001*	0.25 (0.20–0.29)	<0.001*	0.00 (−0.03 to 0.04)	0.905	0.06 (0.03–0.10)	<0.001*
ACR (mg/g)	0.03 (−0.01 to 0.07)	0.089	−0.03 (−0.06 to 0.01)	0.187	−0.06 (−0.10 to −0.02)	0.002*	−0.02 (−0.06 to 0.02)	0.399	0.04 (0.00–0.08)	0.030*	−0.10 (−0.14 to −0.06)	<0.001*
UOB	0.00 (−0.02 to 0.03)	0.882	−0.04 (−0.07 to −0.02)	<0.001*	−0.00 (−0.02 to 0.02)	0.933	0.07 (0.05–0.10)	<0.001*	−0.01 (−0.04 to 0.01)	0.341	−0.01 (−0.03 to 0.01)	0.421
UA (µmol/L)	−0.03 (−0.04 to −0.02)	<0.001*	−0.07 (−0.08 to −0.06)	<0.001*	−0.04 (−0.05 to −0.03)	<0.001*	−0.02 (−0.05 to −0.03)	<0.001*	0.00 (−0.01 to 0.02)	0.384	0.00 (−0.01 to 0.01)	0.904
UMAlb (mg/L)	0.02 (−0.02 to 0.06)	0.284	−0.05 (−0.09 to −0.01)	<0.001*	−0.09 (−0.13 to −0.05)	0.011*	−0.01 (−0.05 to 0.03)	0.525	0.03 (−0.01 to 0.07)	0.123	−0.08 (−0.12 to −0.05)	<0.001*
Cr (µmol/L)	−0.01 (−0.02 to 0.01)	0.351	−0.03 (−0.05 to 0.02)	<0.001*	−0.12 (−0.13 to −0.11)	<0.001*	−0.11 (−0.12 to −0.09)	<0.001*	−0.00 (−0.02 to 0.01)	0.634	−0.07 (−0.08 to −0.05)	<0.001*
Urea (mmol/L)	−0.02 (−0.03 to −0.01)	0.001*	−0.04 (−0.05 to −0.03)	<0.001*	−0.14 (−0.15 to −0.13)	<0.001*	−0.15 (−0.16 to −0.14)	<0.001*	−0.01 (−0.02 to 0.00)	0.289	−0.07 (−0.08 to −0.06)	<0.001*
Alb (g/L)	−0.03 (−0.06 to 0.01)	0.141	−0.12 (−0.15 to −0.09)	<0.001*	−0.21 (−0.24 to −0.18)	<0.001*	−0.17 (−0.21 to −0.14)	<0.001*	−0.02 (−0.05 to 0.01)	0.259	−0.10 (−0.13 to −0.06)	<0.001*

AVR arteriovenous ratio, Df fractal dimension, TORT vascular tortuosity, UWF ultra-wide field, UCr urinary creatinine, ACR urinary albumin-to-creatinine ratio, UOB urine occult blood, UA blood uric acid, UMAlb urinary microalbuminuria, Cr blood creatinine, Urea blood urea, Alb blood albumin.
*P < 0.05.

Table 3 | Subgroup analysis of the correlation between renal function indicators and Df by field range and vascular type

Indicator	Retinal artery				Retinal vein			
	Artery-Center-Df	P-value	Artery-UWF-Df	P-value	Vein-Center-Df	P-value	Vein-UWF-Df	P-value
eGFR	0.20 (0.17–0.22)	<0.001*	0.31 (0.28–0.33)	<0.001*	0.07 (0.05–0.08)	<0.001*	0.22 (0.20–0.25)	<0.001*
UCr (mmol/L)	0.11 (0.07–0.14)	<0.001*	0.24 (0.18–0.27)	<0.001*	0.04 (0.00–0.07)	0.038*	0.23 (0.18–0.26)	<0.001*
ACR (mg/g)	−0.06 (−0.10 to −0.02)	0.003*	−0.06 (−0.10 to −0.02)	0.004*	−0.04 (−0.08 to 0.00)	0.061	0.01 (−0.03 to 0.05)	0.590
UOB	0.01 (−0.02 to 0.03)	0.557	0.07 (0.05–0.09)	<0.001*	−0.02 (−0.05 to 0.00)	0.062	0.06 (0.03–0.08)	<0.001*
UA (µmol/L)	−0.07 (−0.08 to −0.05)	<0.001*	−0.05 (−0.06 to −0.04)	<0.001*	0.01 (−0.00 to 0.02)	0.108	0.03 (0.02–0.04)	<0.001*
UMAlb (mg/L)	−0.08 (−0.12 to −0.04)	<0.001*	−0.05 (−0.09 to −0.01)	0.014*	−0.05 (−0.09 to −0.02)	0.005*	0.02 (−0.02 to 0.05)	0.412
Cr (µmol/L)	−0.14 (−0.16 to −0.13)	<0.001*	−0.14 (−0.15 to −0.13)	<0.001*	−0.04 (−0.05 to −0.03)	<0.001*	−0.06 (−0.07 to −0.05)	<0.001*
Urea (mmol/L)	−0.15 (−0.16 to −0.14)	<0.001*	−0.17 (−0.18 to −0.16)	<0.001*	−0.06 (−0.07 to −0.05)	<0.001*	−0.11 (−0.12 to −0.10)	<0.001*
Alb (g/L)	−0.23 (−0.26 to −0.20)	<0.001*	−0.22 (−0.25 to −0.19)	<0.001*	−0.10 (−0.13 to −0.07)	<0.001*	−0.10 (−0.14 to −0.07)	<0.001*

AVR arteriovenous ratio, Df fractal dimension, TORT vascular tortuosity, UWF ultra-wide field, UCr urinary creatinine, ACR urinary albumin-to-creatinine ratio, UOB urine occult blood, UA blood uric acid, UMAlb urinary microalbuminuria, Cr blood creatinine, Urea blood urea, Alb blood albumin.
*P < 0.05.
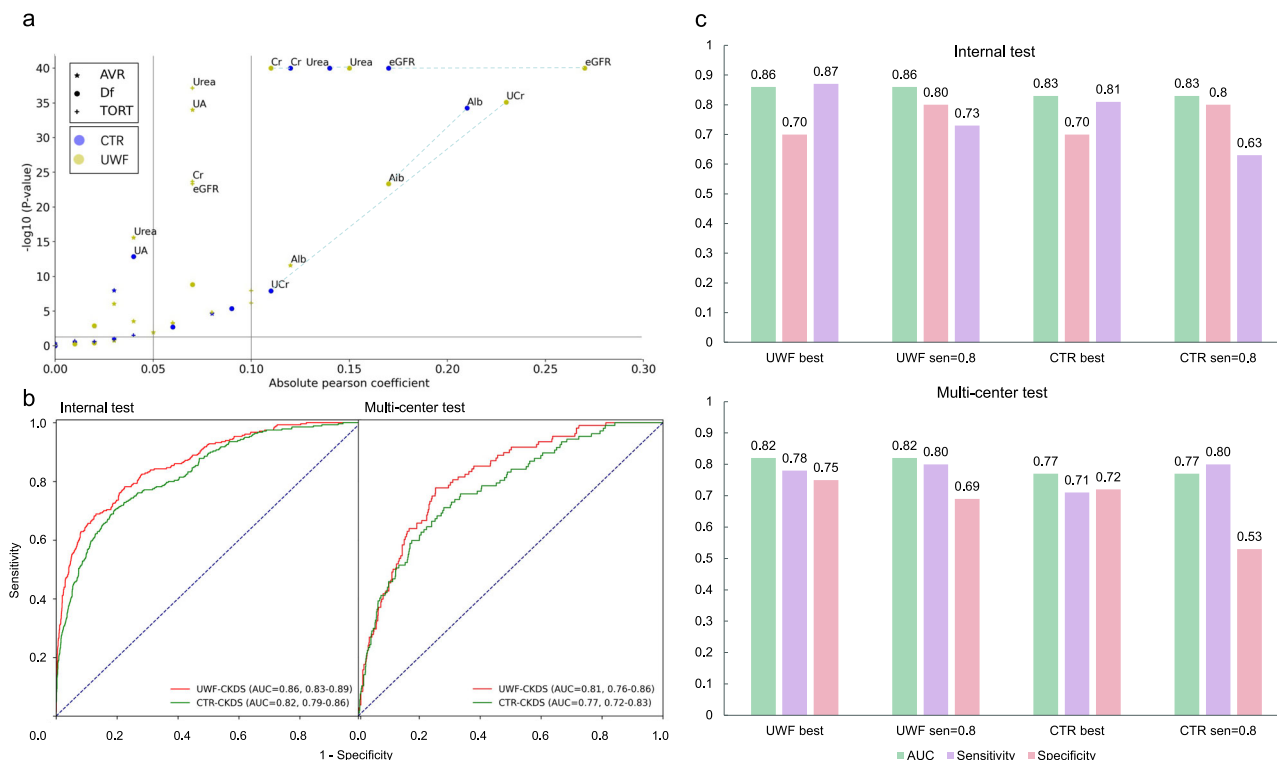
Fig. 3 | Comparison of retinal microvascular parameters-renal function correlation between UWF- and CTR-CKDS models. a *Df* of the UWF or CTR images were significantly correlated with most of the renal function indicators in different level. Generally, the UWF-*Df* showed a better correlation with renal functions than CTR-*Df*. The UWF-*Df* showed the highest correlation coefficient with eGFR. **b** The UWF-CKDS model achieved higher AUC values than the CTR-CKDS model on both test datasets (internal 0.86 95% CI: 0.83–0.89 versus 0.82 95% CI: 0.79–0.86, $P < 0.01$; multicenter 0.81 95% CI: 0.76–0.86 versus 0.77 95% CI: 0.72–0.83, $P = 0.01$). **c** More detailed comparison of AUC, sensitivity, and specificity between UWF- CKDS and CTR-CKDS on both datasets also revealed the better performance of the former model. When the sensitivity value was set at 0.80, UWF-CKDS also showed better specificity than CTR-CKDS in the multicenter test (0.69 95% CI: 0.65–0.71 versus 0.53 95% CI: 0.50–0.56, $P < 0.01$).

Demographic effects on the prediction performance of UWF-CKDS

Since not only the UWF images but also demographic characteristics, like age and sex, were input to the model. Further examination was conducted to explore the impact of these demographic characteristics on the overall model performance. The multi-variable logistic regression showed that sex, age, diabetes, hypertension, and cerebrovascular disease have statistically significant associations with the prediction of CKD (Supplementary Table 2). To further clarify the influence of age and other confounding factors, we conducted age-matched experiments, as well as propensity score matching (PSM) to control for all the above confounders and construct matched training sets. The model trained on the age-matched dataset showed an internal AUC of 0.79 (95% CI: 0.78–0.80) and an external AUC of 0.68 (95% CI: 0.66–0.70), while the model trained on the PSM dataset showed an internal AUC of 0.81 (95% CI: 0.80–0.82) and an external AUC of 0.70 (95% CI: 0.68–0.72). They were only slightly inferior to those of the original UWF-CKDS (internal AUC = 0.86, 95% CI: 0.83–0.89; external AUC = 0.81, 95% CI: 0.76–0.86, see Supplementary Tables 2–4).

Discussion

This prospective, nationwide, multicenter study developed a DLA for CKD screening by UWF fundus images. The vascular segmentation model achieved satisfactory performance in vessel segmentation and RMP measurement. We found UWF-*Df* was significantly correlated with renal functions, especially Artery-UWF-*Df* with eGFR ($r = 0.31$, 95% CI 0.29–0.33). Our UWF-CKDS demonstrated solid predicting ability and suggested peripheral retina could contribute to CKD prediction, as the UWF-CKDS achieved higher AUC than the CTR-CKDS in both internal and multicenter tests. For screening purpose, the specificity of UWF-CKDS

could also be superior when the sensitivity value was set as 0.80, as verified in the multicenter test (0.65 95% CI: 0.62–0.69 versus 0.56 95% CI: 0.53–0.60, $P < 0.01$).

To develop this model, the first step was to achieve automatic and accurate artery/vein segmentation and measurement[2]. However, previous studies focused only on conventional fundus images, segmenting the vessels without distinguishing between arteries and veins, or could not achieve fully automatic calculation of vessel indices for UWF fundus images[25]. Our segmentation model was based on the UNet++ architecture, which introduced dense connections between different levels, allowing the model to capture richer multi-scale features than the previous U-Net architecture, and thus improved the vessel segmentation ability for UWF images[26]. Additionally, our model inputs larger-sized (1024 × 1024) UWF images, better preserving the features of small vessels. We also avoided splitting the entire UWF image into multiple patches for input, as this would severely affect the distinction between arteries and veins. The optic disc channel was used to help mimic ophthalmologists since they typically initiated the arteriovenous differentiation process near the optic disc. As a result, our model could simultaneously segment arteries, veins, and the optic discs for UWF fundus images with high accuracy (AUC = 0.74, 0.80, and 0.94, respectively). The representative images shown in Fig. 2 also demonstrated high consistency between the model and human doctors.

As discussed earlier, the eye and kidney share some structural, physiological, and even pathological similarities[15,27]. Thus, it might be possible that a specific relationship between the two organs can be established by measuring their associated indices, based on which we can further utilize fundus information to predict renal functions. Indeed, in 2020, Xiayu et al. found that for patients with type 2 diabetes, the presence of micro-albuminuria was associated with smaller peripheral arteriolar caliber, larger
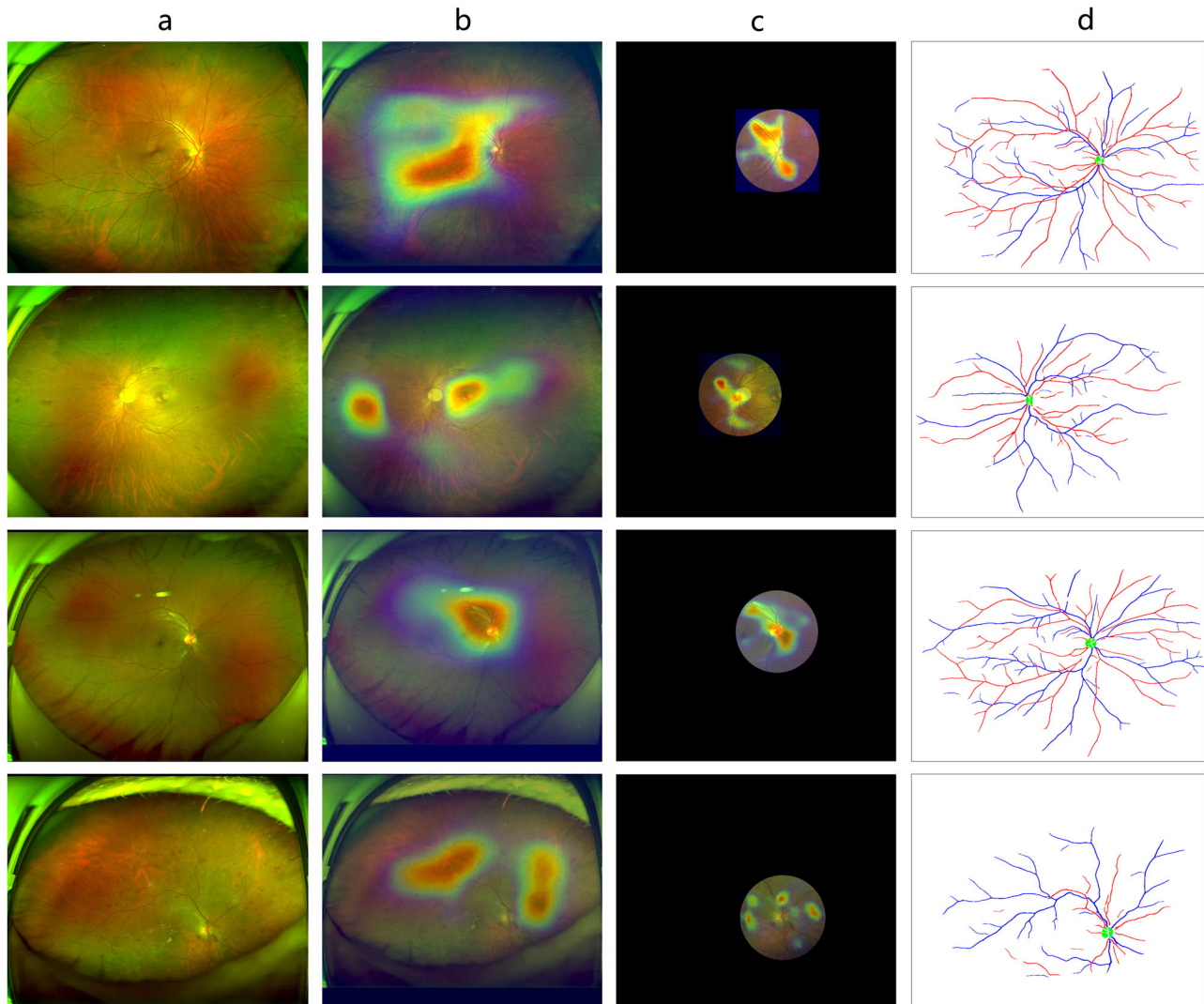
Fig. 4 | Representation and comparison of regions of interest between UWF- and CTR-CKDS models. Four randomly selected images, along with the heatmaps, showed the regions of interest of both UWF- and CTR-CKD models. The UWF- CKDS model focused not only on the posterior pole but also on the peripheral retina. **a** Raw UWF fundus image, **b** region of interest of UWF-CKDS, **c** region of interest of CTR-CKDS, and **d** corresponding extracted vessels and optic disc.

peripheral venular caliber, and smaller arteriolar *Df* in color fundus photographs[22]. These findings verified the above hypothesis and showed the potential of noninvasive RMPs to serve as preclinical markers to identify populations at high risk of early kidney disease. In this study, we assessed the correlation between a series of RMPs and renal function indicators. Results showed significant correlations at varying levels between eGFR, UCr, ACR, UA, UMAlb, Cr, Urea, Alb, and RMPs. Notably, UWF-*Df* exhibited a stronger correlation with eGFR than CTR-*Df*, with Artery-UWF-*Df* showing the highest Pearson correlation coefficient. Our results might provide stronger evidence for the notion mentioned in the former study in several aspects. First, the peripheral vascular changes they claimed were limited in the posterior pole of a traditional fundus photograph, while we calculated the vascular *Df* of the entire UWF image, which contains the true peripheral retina. Moreover, our findings indicated that the correlation between TORT and renal function was predominantly observed in UWF images, as opposed to CTR images. This suggests that peripheral retinal microcirculation may reflect early pathophysiological changes more effectively than the central retina. Second, they classified microalbuminuria as absent or present, while renal function indicators and RMPs in our study were both recorded as continuous variables. Thus, the analyzing results might be more reliable. Third, we included up to 9 renal function indicators and reveal more comprehensive associations between 8 of them and RMPs.

In total, our study demonstrated that a broader fundus area could offer the opportunity to establish a more robust correlation with renal function than traditional fundus images.

When predicting CKD, our UWF-CKDS did outperform CTR-CKDS, showing a higher AUC with reduced variability. To the best of our knowledge, there have been few studies utilizing UFW images to study the relationship between renal functions. Thus, our study pioneers the exploration of the peripheral retina's important value in DLA-based CKD prediction. In a recent study by Sabanayagam et al., a DLA based on traditional color fundus photography achieved good performance for CKD detection in the internal dataset (AUC = 0.911, 95% CI 0.886–0.936), which decreased significantly in two external datasets (AUC = 0.733 and AUC = 0.835, respectively)[24]. In contrast, our UWF-CKDS had a more stable performance between internal (AUC = 0.86, 95% CI 0.83–0.89) and external tests (AUC = 0.81, 95% CI 0.76–0.86). We inferred the much larger number of UWF images used for training our model (*n* = 16,266 versus *n* = 5188 in their study) helped maintain its performance stability. The two models seemed to be similar in the external tests. However, considering the performance of UWF-CKDS was better than that of CTR-CKDS in our study, we thought the different DLA designs in our and Sabanayagam's studies might partially explain their similar external performances. Even though, our model might still potentially be more reliable since the results were based

on the quantified relationship between RMPs and renal functions. To further minish the black-box effect of DLAs and to elucidate the operational distinctions between UWF and CTR image-based models, we used Grad-Cam to highlight areas of interest for both algorithms. UWF-CKDS not only focused on the optic disc region but also covered a larger peripheral retinal area.

When further exploring the role of other demographic features included in the model, we found the contributions of the factors, including sex, age, diabetes, hypertension, and cerebrovascular disease, were significantly smaller than the retinal image features, which means the latter plays a major role in CKD prediction. It is important to note that the main objective of this study is to develop a practical CKD screening tool that integrates various available information to maximize diagnostic efficacy. The confounding factor analysis helps to better understand the sources of information for the model's predictions. This understanding can also guide the interpretation of the model's results and improve its acceptability for clinical usage.

The PUMCH, a national medical center, serves a diverse patient population across China, ensuring the representativeness of our training dataset. Our external dataset was prospectively collected from 23 nationwide tertiary hospitals, encompassing various ethnic groups and remote regions. This means that our model was developed and tested in a real-world clinical environment within a multi-ethnic country, making it well-suited for clinical applications. By comparison, the number of patients included in the former mentioned two studies was relatively limited and one of them was conducted on community-based populations, which might limit their clinical potentials[22,24]. Moreover, our approach is automatic and efficient, eliminating the need for time-consuming and labor-intensive procedures. This makes it ideal for population-level CKD screening. When combined with a vehicle-mounted fundus camera, it can extend its utility at low cost to community and primary care settings, particularly benefiting underserved rural areas with limited medical resources. An additional advantage of using UWF images, as opposed to traditional fundus images, is that it does not require mydriasis, making the process quicker and safer by avoiding potential risks associated with mydriasis. Low-quality UWF images may indicate a need for further ophthalmic assessment, which adds to their screening value.

While the reported DICE scores indicated room for improvement in our arteriovenous segmentation in UWF images, there were some noteworthy issues. First, there was a scarcity of published research on arteriovenous segmentation in UWF images. Most current only focused on the metrics in the posterior region. Second, although some studies reported higher DICE scores based on the 35–55° posterior fundus images, their arteriovenous segmentation was mainly developed and tested in relatively normal and health images[28]. In contrast, our model was developed and tested on 200° UWF images, and most of these patients took the UWF images for certain kinds of ocular abnormalities, such as cataract, vitreous opacity, and severe fundus diseases like retinal artery/vein obstruction, and even proliferative diabetic retinopathy with dense laser spots. Besides, due to much wilder fundus field, the annotation of peripheral artery/vein was extremely difficult. Since it might be inappropriate to directly compare the 200° UWF arteriovenous segmentation with current available studies, we evaluated the metrics in the posterior region. In this area, our segmentation model achieved DICE scores of 0.64 for arteries and 0.70 for veins, with AUC scores of 0.83 and 0.86, respectively. This depicted a significantly improved segmentation accuracy in the most clinically relevant region of the retina.

Our study has limitations. First, though we found significant correlations between renal function indicators and RMP, such as Artery-UWF-*Df* with eGFR, these correlations were relatively modest (up to 0.31), potentially limiting the clinical utility of our findings. Second, our model was developed and tested in a nationwide, large-scale cross-sectional dataset. Prospective follow-up data could enhance the model's performance. Third, though our study included multiple ethnic populations in vast area of China, they were mainly Asians. Data for certain Chinese ethnic minorities and races from other countries, like Caucasians, were still limited. We will try to include patients of more races to further improve the utility of our UWF-CKDS. Lastly, while our UWF-CKDS showed promise in CKD screening, it does not provide quantitative eGFR or CKD stage predictions. It was primarily designed as a binary classification system for innovative screening. Over time, with more data, it may become more efficient and adaptable, potentially evolving to provide quantitative predictions.

In conclusion, the UWF-CKDS trained and tested by a nationwide, multicenter dataset showed solid performance in CKD screening and verified the role of the peripheral retina in predicting renal function. Notably, Artery-UWF-*Df* showed the best correlation with renal function indicators. This noninvasive, automatic, non-mydriatic, and highly adaptable UWF-CKDS offers an innovative and accurate method for population-level CKD screening.

Methods
Study design and participants
This prospective, multicenter study was spearheaded by the Department of Ophthalmology at Peking Union Medical College Hospital (PUMCH) in Beijing, China. The study was carried out in two phases, utilizing clinical data gathered from the ophthalmology departments of 23 tertiary referral hospitals across the nation. The first phase took place from November 1, 2018, to December 1, 2022. During this phase, we initially developed a vascular segmentation model for ultra-wide-field (UWF) fundus images and automatically quantified various retinal microvascular parameters (RMPs), including the fractal dimension (*Df*), vascular tortuosity (TORT), and arteriovenous ratio (AVR). Subsequently, we analyzed the correlation between these RMPs and multiple renal function indices. We then constructed a screening classification model capable of predicting whether a subject had chronic kidney disease (CKD) by inputting UWF images, vascular indicators, basic patient information, and medical history (Fig. 5). To be specific, a 70:15:15 patient-level data split was used for training, validation, and internal testing, respectively. This approach ensured that there was no potential information leakage across these datasets. The second phase of the study was conducted from January 1, 2023, to July 1, 2023. During this stage, we employed a multicenter dataset collected from the 23 medical settings to evaluate the performance of the CKD screening model on a national scale.

Ethical approval for this study was obtained from the Institutional Review Board/Ethics Committee of Peking Union Medical College Hospital (Registration Number: I-22PJ252), the Medical Ethics Committee of Beijing Tsinghua Changgung Hospital, the Ethics Committee of Beijing Tiantan Hospital, the Ethics Committee of Eye Hospital of Shandong First Medical University, the Ethics Committee of Tonghua Eye Hospital of Jilin Province, the Ethics Committee of Guangdong Provincial People's Hospital, the Medical Ethics Committee of Guizhou Provincial People's Hospital, the Medical Ethics Committee of Hunan Provincial People's Hospital, the Ethics Committee of the Fourth People's Hospital of Shenyang, the Ethics Committee of the Affiliated Hospital of Chengde Medical University, the Medical Ethics Committee of the Second Affiliated Hospital of Hebei North University, the Ethics Committee of Xi'an No. 1 Hospital, the Medical Ethics Committee of the First Affiliated Hospital of Kunming Medical University, the Medical Ethics Committee of Renmin Hospital of Wuhan University, the Ethics Committee of the First Hospital of China Medical University, the Ethics Committee of Bayinguoleng people's Hospital, the Ethics Committee of the Affiliated Hospital of Inner Mongolia Medical University, the Medical Ethics Committee of Hainan Hospital of Chinese People's Liberation Army (PLA) General Hospital, the Ethics Committee of the Second Affiliated Hospital of Harbin Medical University, the Ethics Committee of the First Affiliated Hospital of Zhengzhou University, the Ethics Committee of Fujian Medical University Union Hospital, the Ethics Committee of the First Affiliated Hospital of Shanxi Medical University, and the Ethics Committee of the Affiliated Hospital of Southwest Medical University. The study was conducted in accordance with the principles outlined in the Declaration of Helsinki[29]. Written informed consent was obtained from all participating individuals.
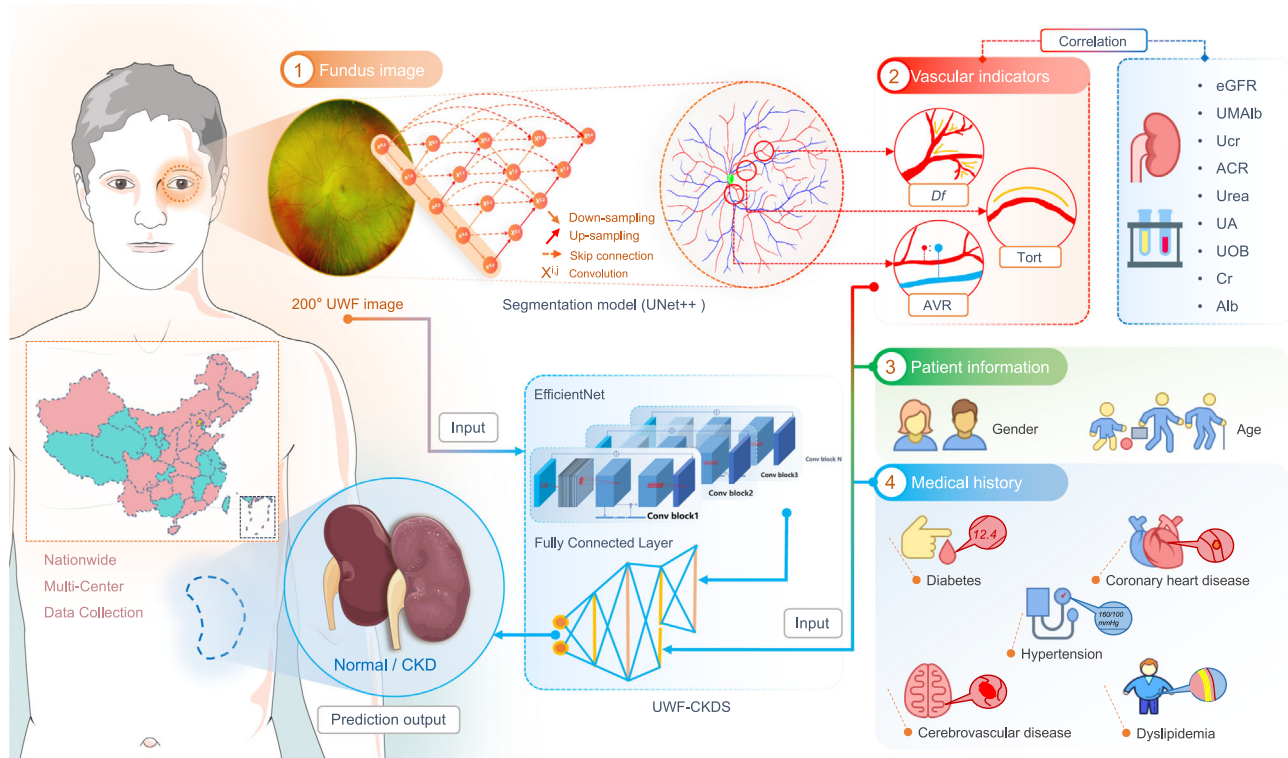
Fig. 5 | Overall input data collection and CKD status prediction procedure. Vascular indices, including the *Df*, TORT and AVR, were measured automatically after segmenting the UWF images with UNet++ based segmenting model. The correlation between the vascular indices and multiple renal function indices was further analyzed. Finally, a classification model, which combines the raw UWF image, 2 items of patient information, 5 items of medical history information, and the 3 items of vascular indicators as the input, generates the prediction output of CKD status (yes or no). This model used the EfficientNet structure to extract image features from UWF images and then employed multi-layer fully connected layers to fuse image features and numerical features.

Bilateral Optos UWF fundus images (Daytona, Optos PLC, Dunfermline, UK) and renal function examinations conducted during this period were independently reviewed by two retinal specialists (XZ and LM). Discrepancies were assessed using kappa statistics, and consensus was reached through discussions with the corresponding author (YC). Inclusion criteria were defined as follows: (1) age above 18 years; (2) possession of at least one Optos image; (3) concurrent renal function examinations performed within 1 week of obtaining the Optos images; (4) availability of comprehensive medical history, including diabetes, hypertension, cerebrovascular disease, coronary heart disease, dyslipidemia, etc.; (5) absence of dialysis treatment, blood replacement, or plasma exchange between image acquisition and laboratory testing; (6) for subjects with multiple clinic visits, only images with an interval of more than 3 months between two visits were included. Exclusion criteria encompassed: (1) images significantly affected by artifacts; (2) blurred images caused by vitreous hemorrhage, astrocytosis, severe cataracts, etc.; (3) images where retinal vessels, the optic disk, and other fundus structures were inadequately displayed; (4) patients who had undergone previous vitreoretinal surgery or retinal photocoagulation; (5) images with excessive brightness or darkness. The evaluation of image quality was conducted by a specially designed artificial intelligence (AI) algorithm[30]. To assess the algorithm's quality control precision in this study, we randomly selected 200 images each from the algorithm's approved and rejected datasets, respectively. Three ophthalmologists independently reviewed these 400 images (200 qualified images and 200 unqualified images), yielding inter-rater consistency scores. The collective verdict from the reviewers established the gold standard through a majority vote. The concordance of each expert with the gold standard was evaluated. Using the gold standard constituted by expert consensus, the model's performance relative to the gold standard in the 2×2 contingency table was subsequently evaluated.

Clinical examinations of renal function and definition of CKD cases

The renal function indicators included in this study were: estimated glomerular filtration rate (eGFR), urinary microalbuminuria (UMAlb), urinary creatinine (UCr), urinary albumin-to-creatinine ratio (ACR), blood urea (Urea), blood uric acid (UA), urine occult blood (UOB), blood creatinine (Cr), and blood albumin (Alb). eGFR was calculated using the Creatinine Plus standardized enzymatic assay and the Chronic Kidney Disease-Epidemiology Collaboration (CKD-EPI) equation[31].

In this study, CKD+ was defined as eGFR <60 mL/min/1.73 m² for more than 90 days, corresponding to CKD stages 3 and above, as defined by the Kidney Disease Improving Global Outcomes (KDIGO) stages of CKD[32]. This definition was supported by medical records or risk factors for renal function impairment. Patients with potential transient renal dysfunction underwent detailed evaluation and confirmation by a renal medicine specialist. Individuals with eGFR ≥60 mL/min/1.73 m² were categorized as controls, corresponding to CKD stages 0 to 2.

Composition of the UWF image segmenting and CKD screening system

Artery/vein segmentation of UWF images. The vessel segmentation model was the UNet++ architecture[26], with EfficientNet B5 serving as the encoder[33]. UNet++ was designed to improve the accuracy of segmentation tasks by introducing nested and dense skip connections, optimizing the original U-Net architecture. This modification enhances gradient flow and allows for more levels of feature fusion within the network, making UNet++ particularly effective in capturing finer anatomical structures such as vessels. EfficientNet was chosen for its efficient use of computational resources and its good scalability across various tasks. With the pre-training based on a large dataset of traditional fundus images, it has shown better performance than other models, like ResNet50 and ViT (Supplementary Table 5). The
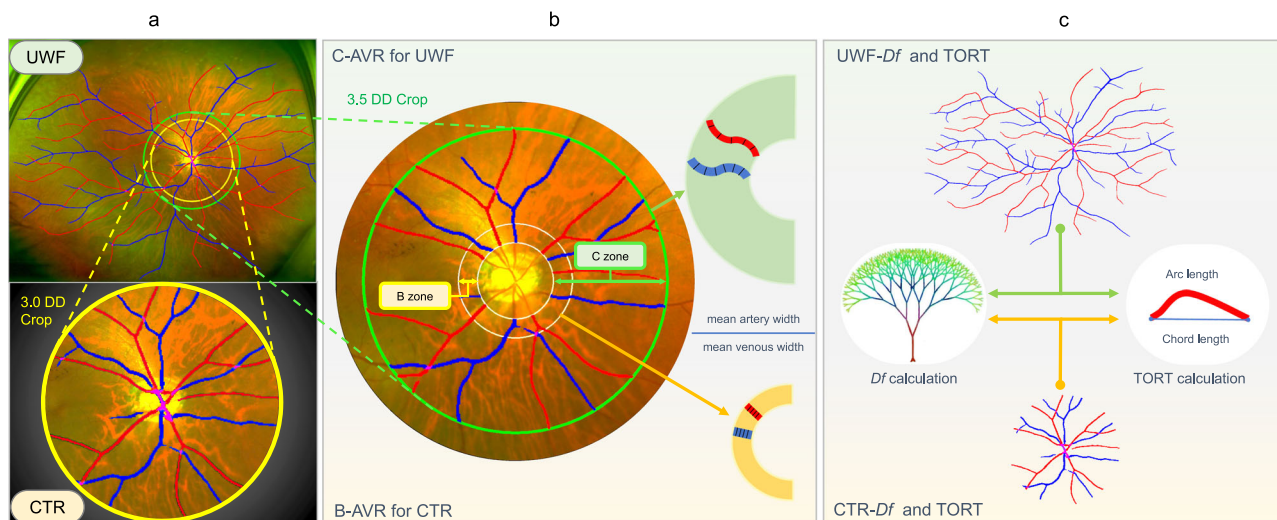
Fig. 6 | Comparison of retinal microvascular parameters between UWF and optic disc-centered image. a An optic disc-centered circular region with a radius of 3 DD away from the optic disc was cropped from the UWF image to represent the central 50° fundus region (denoted as CTR). **b** B-zone (an annular region that is 0.5–1 DD outside the optic disc) and C-zone (an annular region that is 0.5–3.5 DD outside the optic disc) are used for calculating the AVR for CTR and UFW image (denoted as B-AVR and C-AVR, respectively). **c** The Df and TORT of both CTR and UWF images were also calculated and compared.

model ultimately generated three distinct channels, corresponding to arteries, veins, and the optic discs. We utilized the Dice Loss function as the loss function[34]. To strengthen the segmentation ability of small blood vessels, and to better distinguish arteriovenous vessels, we initially padded the UWF image into a square shape based on the longer side, followed by scaling it to a fixed, larger size (1024 × 1024). After normalizing the image, it was input into the vessel segmentation model. Metrics used to evaluate the segmentation results included the dice coefficient (DICE) and AUC. DICE = 2*TP/(2*TP + FP + FN) where TP, TN, FP, and FN are the number of true positive, true negative, false positive, and false negative image pixels, respectively. In image segmentation, we could treat each pixel as a sample and draw the ROC curve based on the probability of each pixel belonging to the target object. The maximum values for both DICE and AUC are 1. The larger the value, the better the model's segmentation performance.

The vessel segmentation dataset comprised 218 UWF fundus images annotated by experienced ophthalmology experts, of which 184 images were utilized for training purposes, while the remaining 34 images served as the validation data. We initially pre-trained the model on conventional fundus images and subsequently fine-tuned it on the annotated UWF fundus images. During the fine-tuning process, a plethora of data augmentation techniques were employed, such as random flipping, random adjustments of brightness, saturation, and contrast. The model was implemented using PyTorch and trained for 200 epochs on an NVIDIA TITAN RTX GPU. The Adam optimizer was employed, with a learning rate of 1e-4.

Measurement of retinal vascular metrics. By segmenting the optic disc, retinal arteries, and retinal veins according to their shapes, vascular indices could be obtained automatically. The Df was calculated using the box-counting method, which began by dividing the selected blood vessel mask image into small squares, each with a side length of r. The number of squares covering the vascular structure was calculated and denoted as N(r). Linear regression was then employed to fit N(r) and r, and the resulting slope represented the desired Df. The curvature of blood vessels was measured by simple tortuosity (sTORT). The sTORT calculation method involves initially segmenting the vessel from its branching points into individual segments. Then, the actual length of each segment is measured and divided by the Euclidean distance between its endpoints to find the ratio of the arc to the chord length. Subsequently, these values of each vessel segment are averaged to determine the image's tortuosity. To further study the association between the peripheral retinal area and renal functions, we extracted the central region (denoted as CTR) from the original UWF images, which roughly

correspond to the field of view observed by a traditional 50° fundus camera. We calculated Df (UWF/CTR-Df) and TORT (UWF/CTR-TORT) for the whole images (Fig. 6c). For AVR, we first excluded small branching vessels and calculated the ratio by dividing the mean width of selected arteries by the mean width of selected veins in two annular regions: one was the B-zone near the optic disc (0.5–1 DD outside the optic disc), and the other was the wider C-zone (0.5–3.5 DD outside the optic disc), denoted as B-AVR and C-AVR, respectively. The calculation of blood vessel diameter involves selecting main arteries and three main veins and was then measured at positions perpendicular to the direction of the vessels, with the measurements taken multiple times (Fig. 6b, right part). To obtain the CTR image, we cropped the UWF image by drawing a circle around the center of the optic disc, which was defined as the centroid of the circumscribed circle of the optic disc. The circle was 3 DD away from the optic disc. (Fig. 6a, b).

CKD screening classification model. We developed a deep learning-based and UWF fundus image-based CKD screening classification model (UWF-CKDS). The model first input one UWF fundus image and used three fully connected layers to fuse the extracted image features and other input numerical features, ultimately outputting the probability of CKD+ for that UWF image. The numerical features included patient information (gender, age), medical history (diabetes, hypertension, cerebrovascular disease, coronary heart disease, dyslipidemia), and vascular indices (UWF-Df, UWF-TORT, and C-AVR). The dimensions of three fully connected layers were set to 26, 64, 32, and 2, respectively. Additionally, we trained another classification model (CTR-CKDS) for comparison, which input the CTR image and vascular indices (CTR-Df, CTR-TORT, and B-AVR), while other numerical features were the same with UWF-CKDS. Both models used EfficientNet B3, with the initial weights derived from ImageNet and an internal fundus image dataset pre-training, and a fixed input image resolution of 512 × 512. The loss function was Focal Loss[35]. The model was implemented in PyTorch, trained for 50 epochs on an NVIDIA TITAN RTX, using the Adam optimizer with a learning rate of 6e-4.

Statistical analysis
For continuous variables, we calculated means and standard deviations (SD). To assess the relationships between renal function indicators (eGFR, UMAlb, UCr, ACR, Urea, UA, UOB, Cr, and Alb) and retinal vascular indices (UWF-Df, UWF-TORT, C-AVR, CTR-Df, CTR-TORT, and B-AVR), we computed Pearson correlation coefficients (r) and their 95% confidence intervals (CI). A P-value below 0.05 indicated statistical

significance. To evaluate the CKD screening model, we determined the area under the receiver operating characteristic (ROC) curve (AUC). The model's classification threshold was set at 0.5, classifying instances with probabilities exceeding 0.5 as positive outcomes. We also computed the confusion matrix for both internal and external test sets to better assess the performance. To visualize the areas of interest within the images associated with renal function, we used Grad-CAM 28 for representation.

Data availability

Individual participant data will be made available on request, directed to the corresponding author (Y.C.). After approval by the Institutional Review Board/Ethics Committee of PUMCH, partial data can be shared through a secure online platform for research purposes. Given that many aspects of the deep learning system, such as data generation and model training, have a large number of dependencies on internal tooling, infrastructure, and hardware, we are unable to publicly release this code in the current stage.

References

1. Fox, C. S. et al. Associations of kidney disease measures with mortality and end-stage renal disease in individuals with and without diabetes: a meta-analysis. *Lancet* **380**, 1662–1673 (2012).
2. Zhao, X. et al. Relationships between retinal vascular characteristics and renal function in patients with type 2 diabetes mellitus. *Transl. Vis. Sci. Technol.* **10**, 20 (2021).
3. GBD Chronic Kidney Disease Collaboration. Global, regional, and national burden of chronic kidney disease, 1990–2017: a systematic analysis for the Global Burden of Disease Study 2017. *Lancet* **395**, 709–733 (2020).
4. Jha, V. et al. Chronic kidney disease: global dimension and perspectives. *Lancet* **382**, 260–272 (2013).
5. Vanholder, R. et al. Reducing the costs of chronic kidney disease while delivering quality health care: a call to action. *Nat. Rev. Nephrol.* **13**, 393–409 (2017).
6. Ene-Iordache, B. et al. Chronic kidney disease and cardiovascular risk in six regions of the world (ISN-KDDC): a cross-sectional study. *Lancet Glob. Health* **4**, e307–e319 (2016).
7. Tonelli, M. & Dickinson, J. A. Early detection of CKD: implications for low-income, middle-income, and high-income countries. *J. Am. Soc. Nephrol.* **31**, 1931–1940 (2020).
8. Manski-Nankervis, J.-A. E. et al. Screening and diagnosis of chronic kidney disease in people with type 2 diabetes attending Australian general practice. *Aust. J. Prim. Health* **24**, 280–286 (2018).
9. Shlipak, M. G. et al. The case for early identification and intervention of chronic kidney disease: conclusions from a Kidney Disease: Improving Global Outcomes (KDIGO) Controversies Conference. *Kidney Int.* **99**, 34–47 (2021).
10. Poggio, E. D. et al. Systematic review and meta-analysis of native kidney biopsy complications. *Clin. J. Am. Soc. Nephrol.* **15**, 1595–1602 (2020).
11. Saunders, M. R., Cifu, A. & Vela, M. Screening for chronic kidney disease. *JAMA* **314**, 615–616 (2015).
12. Hallan, S. I. et al. Screening strategies for chronic kidney disease in the general population: follow-up of cross sectional health survey. *BMJ* **333**, 1047 (2006).
13. Farrah, T. E., Dhillon, B., Keane, P. A., Webb, D. J. & Dhaun, N. The eye, the kidney, and cardiovascular disease: old concepts, better tools, and new horizons. *Kidney Int.* **98**, 323–342 (2020).
14. Yip, W. et al. Comparison of common retinal vessel caliber measurement software and a conversion algorithm. *Transl. Vis. Sci. Technol.* **5**, 11 (2016).
15. Barrios, C. et al. Circulating metabolic biomarkers of renal function in diabetic and non-diabetic populations. *Sci. Rep.* **8**, 15249 (2018).
16. Ahola-Olli, A. V. et al. Circulating metabolites and the risk of type 2 diabetes: a prospective study of 11,896 young adults from four Finnish cohorts. *Diabetologia* **62**, 2298–2309 (2019).
17. Theuerle, J. D. et al. Retinal microvascular function predicts chronic kidney disease in patients with cardiovascular risk factors. *Atherosclerosis* **341**, 63–70 (2022).
18. Wu, I. W. et al. Retinal neurovascular changes in chronic kidney disease. *Acta Ophthalmol.* **98**, e848–e855 (2020).
19. Mulè, G., Vadalà, M., Geraci, G. & Cottone, S. Retinal vascular imaging in cardiovascular medicine: new tools for an old examination. *Atherosclerosis* **268**, 188–190 (2018).
20. McKay, G. J. et al. Retinal microvascular parameters are not associated with reduced renal function in a study of individuals with type 2 diabetes. *Sci. Rep.* **8**, 3931 (2018).
21. Yip, W. et al. Retinal vascular imaging markers and incident chronic kidney disease: a prospective cohort study. *Sci. Rep.* **7**, 9374 (2017).
22. Xu, X. et al. Comprehensive retinal vascular measurements: a novel association with renal function in type 2 diabetic patients in China. *Sci. Rep.* **10**, 13737 (2020).
23. Wang, S. B. et al. A spectrum of retinal vasculature measures and coronary artery disease. *Atherosclerosis* **268**, 215–224 (2018).
24. Sabanayagam, C. et al. A deep learning algorithm to detect chronic kidney disease from retinal photographs in community-based populations. *Lancet Digit. Health* **2**, e295–e302 (2020).
25. Liu, W. et al. Full-resolution network and dual-threshold iteration for retinal vessel and coronary angiograph segmentation. *IEEE J. Biomed. Health Inf.* **26**, 4623–4634 (2022).
26. Zhou, Z., Siddiquee, M. M. R., Tajbakhsh, N. & Liang, J. UNet++: redesigning skip connections to exploit multiscale features in image segmentation. *IEEE Trans. Med. Imaging* **39**, 1856–1867 (2020).
27. Vadalà, M. et al. Retinal and choroidal vasculature changes associated with chronic kidney disease. *Graefes Arch. Clin. Exp. Ophthalmol.* **257**, 1687–1698 (2019).
28. Hatamizadeh, A. et al. RAVIR: a dataset and methodology for the semantic segmentation and quantitative analysis of retinal arteries and veins in infrared reflectance imaging. *IEEE J. Biomed. Health Inf.* **26**, 3272–3283 (2022).
29. World Medical Association. World Medical Association Declaration of Helsinki: ethical principles for medical research involving human subjects. *JAMA* **310**, 2191–2194 (2013).
30. Zhang, Y. et al. Artificial intelligence-enabled screening for diabetic retinopathy: a real-world, multicenter and prospective study. *BMJ Open Diabetes Res. Care* **8**, e001596 (2020).
31. Levey, A. S. et al. A new equation to estimate glomerular filtration rate. *Ann. Intern. Med.* **150**, 604–612 (2009).
32. Levey, A. S. et al. Definition and classification of chronic kidney disease: a position statement from Kidney Disease: Improving Global Outcomes (KDIGO). *Kidney Int.* **67**, 2089–2100 (2005).
33. Tan, M. & Le, Q. EfficientNet: rethinking model scaling for convolutional neural networks. *PMLR* **97**, 6105–6114 (2019).
34. Sudre, C. H., Li, W., Vercauteren, T., Ourselin, S. & Jorge Cardoso, M. *Deep Learning in Medical Image Analysis and Multimodal Learning for Clinical Decision Support* (eds Jorge Cardoso, M. et al.) 240–248 (Springer, 2017).
35. Lin, T. Y., Goyal, P., Girshick, R., He, K. & Dollár, P. Focal loss for dense object detection. In *Proc. 2017 IEEE International Conference on Computer Vision (ICCV)*, 2999–3007 (2017).

Author contributions

X.Z. and Y.C. (PUMCH) contributed to the concept of the study. X.Z., X.G., L.M., Q.Z., S.C., W.Z., T.C., and C.W. designed the study and did the literature search. G.J., D.T., X.S., B.Z., Y.L., H.L., C.C., H.Z. (The Fourth

People's Hospital of Shenyang), L.Y., C.S. (Affiliated Hospital of Chengde Medical University), H.Z. (The First Hospital of China Medical University), S.X., A.L., M.L., D.Z. (The Affiliated Hospital of Inner Mongolia Medical University), M.X., D.S., Q.L., Z.Z., D.Z. (The First Affiliated Hospital of Shanxi Medical University), H.L., and R.A. collected the data. Y.C. (VoxelCloud), Z.W., S.J., and C.J. contributed to the design of the statistical analysis plan. X.Z., X.G., and L.M. did the data analysis and data interpretation. X.Z. and X.G. drafted the manuscript. C.S. (Singapore Eye Research Institute), T.Y.W., X.D., and Y.C. (PUMCH) critically reviewed and revised the manuscript. X.Z. and Y.C. (PUMCH) provided research funding, coordinated the research, and oversaw the project. All authors had access to all the raw datasets and the corresponding authors (X.D., T.Y.W., and Y.C.) verified the data and made the final decision to submit for publication. All authors reviewed and approved the final manuscript. In this study, X.Z. and X.G. are listed as the co-first authors as they contributed the most to the study. The order of authorship was determined based on individual contributions and confirmed by corresponding authors.

Competing interests
The authors declare no competing interests.

Additional information
Supplementary information The online version contains supplementary material available at https://doi.org/10.1038/s41746-024-01271-w.

Correspondence and requests for materials should be addressed to Xiaowei Ding, Tien Yin Wong or Youxin Chen.

Reprints and permissions information is available at http://www.nature.com/reprints

Publisher's note Springer Nature remains neutral with regard to jurisdictional claims in published maps and institutional affiliations.

[1]Department of Ophthalmology, Peking Union Medical College Hospital, Chinese Academy of Medical Sciences, Beijing, China and Key Lab of Ocular Fundus Diseases, Chinese Academy of Medical Sciences, Beijing, China. [2]Department of Research, VoxelCloud, Shanghai, China. [3]Tonghua Eye Hospital of Jilin Province, Tonghua, Jilin, China. [4]Department of Ophthalmology, Beijing Tiantan Hospital, Capital Medical University, Beijing, China. [5]Eye Hospital of Shandong First Medical University (Shandong Eye Hospital), Jinan, Shandong, China. [6]Department of Ophthalmology, Hunan Provincial People's Hospital, The First Affiliated Hospital of Hunan Normal University, Changsha, Hunan, China. [7]Department of Ophthalmology, The Second Affiliated Hospital of Hebei North University, Zhangjiakou, Hebei, China. [8]Department of Ophthalmology, Xi'an No. 1 Hospital, Xian, Shanxi, China. [9]Eye Center, Renmin Hospital of Wuhan University, Wuhan, Hubei, China. [10]Department of Ophthalmology, The Fourth People's Hospital of Shenyang, China Medical University, Shenyang, Liaoning, China. [11]Department of Ophthalmology, The First Affiliated Hospital of Kunming Medical University, Kunming, Yunnan, China. [12]Department of Ophthalmology, Affiliated Hospital of Chengde Medical University, Chengde, Hebei, China. [13]Department of Ophthalmology, The First Hospital of China Medical University, Shenyang, Liaoning, China. [14]Department of Ophthalmology, Guizhou Provincial People's Hospital, Guiyang, Guizhou, China. [15]Guangdong Eye Institute, Department of Ophthalmology, Guangdong Provincial People's Hospital (Guangdong Academy of Medical Sciences), Southern Medical University, Guangzhou, Guangdong, China. [16]Eye Center, Beijing Tsinghua Changgung Hospital, Beijing, China and School of Clinical Medicine, Tsinghua University, Beijing, China. [17]Department of Ophthalmology, The Affiliated Hospital of Inner Mongolia Medical University, Huhhot, Inner Mongolia, China. [18]Department of Ophthalmology, Hainan Hospital of PLA General Hospital, Sanya, Hainan, China. [19]Department of Ophthalmology, The Second Affiliated Hospital, Harbin Medical Medical, Harbin, Heilongjiang, China. [20]Department of Ophthalmology, The First Affiliated Hospital of Zhengzhou University, Zhengzhou, Henan, China. [21]Department of Ophthalmology, Fujian Medical University Union Hospital, Fuzhou, Fujian, China. [22]Department of Ophthalmology, The First Affiliated Hospital of Shanxi Medical University, Taiyuan, Shanxi, China. [23]Department of Ophthalmology, The Affiliated Hospital of Southwest Medical University, Luzhou, Sichuan, China. [24]Department of Ophthalmology, Bayinguoleng People's Hospital, Korla, Xinjiang, China. [25]Microsoft Research Asia (Shanghai), Shanghai, China. [26]Singapore Eye Research Institute, Singapore and National Eye Centre, Singapore, Singapore. [27]Department of Electrical Engineering, Shanghai Jiao Tong University, Shanghai, China. [28]Tsinghua Medicine, Tsinghua University, Beijing, China. [29]These authors contributed equally: Xinyu Zhao, Xingwang Gu. ✉e-mail: dingxiaowei@sjtu.edu.cn; wongtienyin@tsinghua.edu.cn; ChenYX@pumch.cn